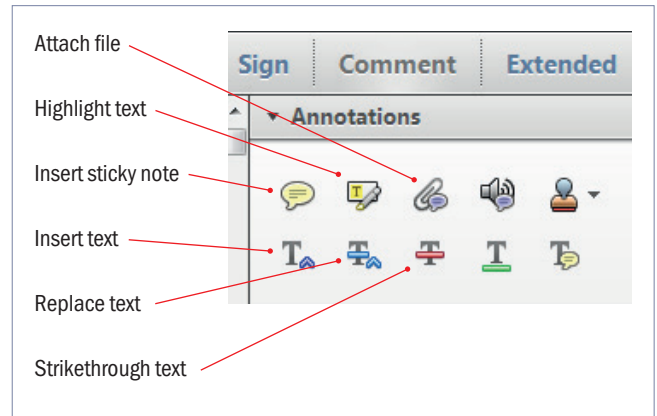


Making corrections to your proof

Please follow these instructions to mark changes or add notes to your proof. Ensure that you have downloaded the most recent version of Acrobat Reader from <https://get.adobe.com> so you have access to the widest range of annotation tools.

The tools you need to use are contained in **Annotations** in the **Comment** toolbar. You can also right-click on the text for several options. The most useful tools have been highlighted here. If you cannot make the desired change with the tools, please insert a sticky note describing the correction.

Please ensure all changes are visible via the 'Comments List' in the annotated PDF so that your corrections are not missed.

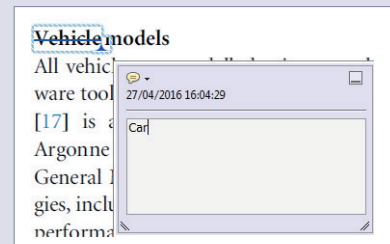


Do not attempt to directly edit the PDF file as changes will not be visible.



Replacing text

To replace text, highlight what you want to change then press the replace text icon, or right-click and press 'Add Note to Replace Text', then insert your text in the pop up box. Highlight the text and right click to style in bold, italic, superscript or subscript.



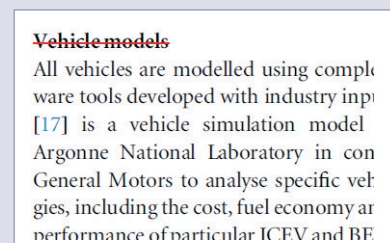
Inserting text

Place your cursor where you want to insert text, then press the insert text icon, or right-click and press 'Insert Text at Cursor', then insert your text in the pop up box. Highlight the text and right click to style in bold, italic, superscript or subscript.



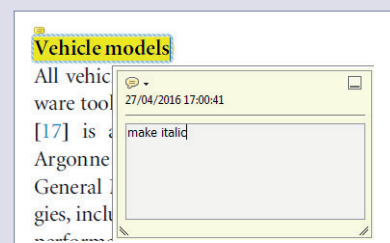
Deleting text

To delete text, highlight what you want to remove then press the strikethrough icon, or right-click and press 'Strikethrough Text'.



Highlighting text

To highlight text, with the cursor highlight the selected text then press the highlight text icon, or right-click and press 'Highlight text'. If you double click on this highlighted text you can add a comment.



QUERY FORM

JOURNAL: Smart Materials and Structures

AUTHOR: B Cowan and P R von Lockette

TITLE: Fabrication, characterization, and heuristic trade space exploration of magnetically actuated Miura-Ori origami structures

ARTICLE ID: smsaa5a9e

The layout of this article has not yet been finalized. Therefore this proof may contain columns that are not fully balanced/matched or overlapping text in inline equations; these issues will be resolved once the final corrections have been incorporated.

Please check that the names of all authors as displayed in the proof are correct, and that all authors are linked correctly to the appropriate affiliations. Please also confirm that the correct corresponding author has been indicated.

If an explicit acknowledgment of funding is required, please ensure that it is indicated in your article. If you already have an Acknowledgments section, please check that the information there is complete and correct.

SQ1

Please be aware that the colour figures in this article will only appear in colour in the online version. If you require colour in the printed journal and have not previously arranged it, please contact the Production Editor now.

Please check that the funding information below is correct for inclusion in the article metadata.
Division of Emerging Frontiers in Research and Innovation: 1240459; Division of Civil, Mechanical and Manufacturing Innovation: 0927326.

Page 1

Q1

Please specify the corresponding author and provide his/her email address.

Page 13

Q2

Please check the details for any journal references that do not have a link as they may contain some incorrect information. If any journal references do not have a link, please update with correct details and supply a Crossref DOI if available. 

Page 13

Q3

Please provide the page range or article number in references [2, 3, 5, 8, 10, 23]. 

Page 14

Q4

References [19, 20] are listed in the reference list but not cited in the text. Please cite in the text, else delete from the list.

Fabrication, characterization, and heuristic trade space exploration of magnetically actuated Miura-Ori origami structures

Brett Cowan¹ and Paris R von Lockette²

¹ 1300 Independence Place Drive—312B, Hinesville GA 31313, United States of America

Q1 ² Penn State University, 160 Hammond Bldg., University Park PA 16802, United States of America

Received 10 August 2016, revised 8 January 2017

Accepted for publication 19 January 2017

Published DD MM 2017



CrossMark

Abstract

The authors develop magnetically actuated Miura-Ori structures through observation, experiment, and computation using an initially heuristic strategy followed by trade space visualization and optimization. The work is novel, especially within origami engineering, in that beyond final target shape approximation, Miura-Ori structures in this work are additionally evaluated for the shape approximation while folding and for their efficient use of their embedded actuators. The structures consisted of neodymium magnets placed on the panels of silicone elastomer substrates cast in the Miura-Ori folding pattern. Initially four configurations, arrangements of magnets on the panels, were selected based on heuristic arguments that (1) maximized the amount of magnetic torque applied to the creases and (2) reduced the number of magnets needed to affect all creases in the pattern. The results of experimental and computational performance metrics were used in a weighted sum model to predict the optimum configuration, which was then fabricated and experimentally characterized for comparison to the initial prototypes. As expected, optimization of magnet placement and orientation was effective at increasing the degree of theoretical useful work. Somewhat unexpectedly, however, trade space results showed that even after optimization, the configuration with the most number of magnets was least effective, per magnet, at directing its actuation to the structure's creases. Overall, though the winning configuration experimentally outperformed its initial, non-optimal counterparts, results showed that the choice of optimum configuration was heavily dependent on the weighting factors. These results highlight both the ability of the Miura-Ori to be actuated with external magnetic stimuli, the effectiveness of a heuristic design approach that focuses on the actuation mechanism, and the need to address path-dependent metrics in assessing performance in origami folding structures.

Keywords: origami engineering, trade space, Miura, optimization, magnetic actuation

SQ1 (Some figures may appear in colour only in the online journal)

1. Introduction

Origami engineering, which applies concepts of origami (origami mathematics, structural and kinematic properties of various fold patterns, target shape approximation and path planning methodologies, etc) to the design of engineering devices, is a relatively new research topic that has seen use in a range of technical applications. Historically the realm of hand-folded paper structures, the movement of origami into the application realm, especially the advent of self-actuated

structures, forces one to consider traditional metrics of engineered systems. While much emphasis in origami engineering has focused on the kinematics, primarily target shape approximation (how well does the folded structure approximate the desired shape?) and motion planning (how can one develop a viable crease and non-intersecting folding pattern to approximate the target shape?) less emphasis has been placed on the efficacy of these structures with respect to the efficiency of their actuation and the degree to which they follow the proscribed folding paths.

This work examines the efficiency of self-actuated origami structures by looking at the degree to which the work performed by their embedded actuators affects their ability to achieve their desired target shape. Target shape, a traditional metric, compares desired fold angles across structures as they deform to their theoretical values. Efficiency, however, is defined as the degree to which the work performed by the embedded actuators is aligned with the theoretical motion through the range of deformation as the crease patterns deforms into its target shape. This study is intended to highlight trade-offs between shape approximation and the efficient utilization of embedded actuators to broaden the discussion on self-actuated origami structures beyond the achievement of target shapes. Additionally, metrics of the degree to which the structures followed their proscribed folding paths are examined.

Many examples of the use of traditional origami patterns in engineering exist. Structures that use origami folding patterns such as the water bomb for medical stents, safety features such as automobile airbags, and multiple flasher patterns for deployable arrays for satellites [1, 2] are but a few instances. Moving away from the historical basis in paper, the media used for these origami structures come from a variety of materials, such as thin sheets of metal or plastic, which can be tailored, especially in the geometry around desired fold lines, to provide the desired behavior. This tailoring often includes notches, cutouts, etc to promote localized folding or to remove physical barriers to folding such as self-interaction [1]. Furthermore, researchers are developing means of using external stimuli to actuate the folds as opposed to traditional by-hand folding.

The actuation by external stimuli can range from a wide variety of options, including electric fields, magnetic fields, heat, and mechanical pressure. Ryu *et al* [3] used polymers with residual photoabsorbing molecules and photomechanically programmed a six-sided box shape from a rectangular sheet that folded once it was cut from the sheet. Martinez *et al* [4] created and tested Ecoflex-paper composites containing a pneumatic channel of various design, exemplifying their possible use as actuators by way of pressurization. Okuzaki *et al* [5] were able to create a biomorphic origami robot capable of caterpillar-like motion and an accordion-shaped origami actuator that were both actuated by an electric field. Von Lockette and Sheridan [6] created and modeled a composite magnetically-actuated elastomer (MAE)/PDMS accordion structure that deformed reversibly in a magnetic field. Bowen *et al* [7] has sought to actuate more complex origami structures, particularly the waterbomb base and the frog's tongue by way of magnetic material and a magnetic field.

While a range of actuating mechanisms exist, this work will focus on the study of origami actuated using external magnetic fields interacting with neodymium magnets. The magnets, placed strategically within the origami folding pattern, act as localized primarily torque-based actuators producing the required motion at the creases. Neodymium magnets have been utilized as actuators in previous works, such as in a planar actuator [8] and in a MEMS actuator [9]. Magnetic fields were chosen for actuation due to their

bidirectionality (the ability to fold actively reversibly) a trait not present among other stimuli-responsive materials such as dielectric elastomers, terpolymers, electrostrictive polymers, SMAs, shape memory polymers, and even soft-magnetic MAEs. Magnetic fields have a relatively fast response time (0–0.1 s), which surpasses that of SMA and photo-thermal polymer medium response times (0.1–0.5 s) and that of shape memory polymer and photochemical polymers with even slower response times (>0.5 s) [10]. An added benefit of magnetic field actuation is the absence of leads and wires, unlike electric field actuation where these are required. Magnetic field actuation, however, does require structures to remain in the field to actuate them, a limitation in some instances, but one that allows for *in situ* applications.

Magnetic field actuation will be employed to fold the Miura-Ori pattern, a rigid origami pattern comprised of identical parallelogram facets surrounding degree four vertices [11, 12]. The inherent properties of the Miura-Ori, which include 1-DOF tessellation, reduced folding stresses compared to orthogonal folding, and equal magnitude but opposite sign Poisson's ratios for in-plane and out-of-plane deformations, have recently garnered increased interest in its use in engineering applications. Horner [13] tested a deployment method of a Miura-Ori experimental solar sail model utilizing four inflatable struts. Lui *et al* [14] created a Miura-Ori patterned sheet out of Elvaloy and detailed its mechanical response in out-of-plane and in-plane direction compression tests and three-point bending tests. From the tests, it was shown that the patterned sheets mostly returned to their original dimensions, suggesting repeatable uses. Schenk and Guest [15] introduced two folded metamaterials, engineered smart materials possessing properties not found within nature, which were based on the Miura-Ori pattern. The folded cellular metamaterial was capable of self-locking into a prescribed configuration, which could provide a specific stiffening response to an applied load. While these previous works have investigated the performance of specific active Miura-Ori structures, none have attempted to describe a framework for optimization of the desired actuation. Results are given for the structures tested with respect to the desired response, but none seek to neither optimize the actuating mechanism itself nor ascertain the degree to which the structures adhere to the proscribed folding paths.

In this work, the ability of neodymium magnets to actuate a Miura-Ori pattern will be investigated with regard to the arrangements of the magnets within the pattern. The dominant mode of magnetic actuation will be through the generation of magnetic torque acting on individual magnets following

$$\mathbf{T} = \mathbf{m} \times \mathbf{H}, \quad (1)$$

where \mathbf{T} is the magnetic torque density generated, \mathbf{m} is the magnetization of the magnet, and \mathbf{H} is the applied external field strength. Torque effects are considered dominant due to

- (1) the use of a nominally uniform magnetic field which makes external-field-induced gradients at least symmetric

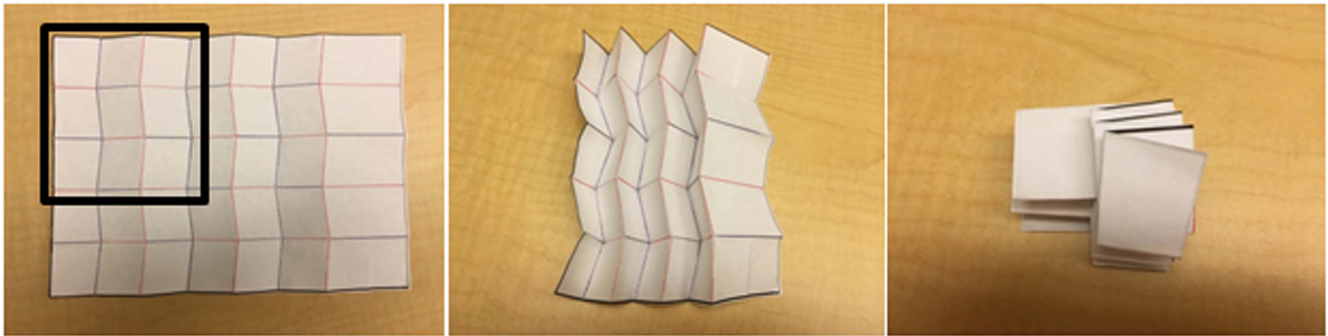


Figure 1. A paper Miura-Ori design as it goes from its initial flat state to its completely folded state, from left to right. The mountain folds are shown as red lines and the valley folds are shown as blue lines. The black highlighted region is the smallest possible iteration of this origami structure.

with respect to the magnet, hence removing magnetic forces due to the external field;

- (2) the initial spacing of the magnets on the structure that show no attraction (movement) toward one another;
- (3) the ability of the structure to relax into its undeformed state when the external field is removed, which suggests that inter-magnet forces are minimal when compared to the elastic behavior of the structure over the range of deformations tested.

Miura-Ori structures having magnets placed on various panels and in various orientations on the panels will be analyzed using a combination of experimentation and simulation. The placement and orientation parameters will constitute a design space that will be systematically explored to develop an optimized pairing of magnetic placement and orientation to maximize performance metrics. Included in these metrics are calculations that estimate the theoretical magnetic work applied to the Miura-Ori's creases, the ability of the proposed structure to follow the prescribed Miura-Ori folding behavior, and the structure's degree of folding.

2. Methodology

2.1. Design and fabrication of Miura-Ori substrates

The Miura-Ori fold, more commonly called the Map Fold, consists of an alternating design of mountain and valley folds and parallelogram/trapezoidal-shaped panels whose crease pattern is actuated by grabbing opposing corners and bringing them to one another. The design of this structure can be seen in figure 1, with the smallest viable iteration of the Miura-Ori boxed in black. The creases that run almost vertically in a symmetric alternating pattern, which will be referred to as the vertical creases, do not have a prescribed angle from the vertical in the Miura-Ori structure; they may be chosen by the designer. However, these vertical creases must be angled greater than zero degrees from the vertical and less than 90° from the vertical in order for the Miura-Ori to fold properly. In this work, the Miura-Ori design will have vertical creases that are six degrees from the vertical as shown in figure 2. A

six-degree angle was chosen as it one of the more difficult Miura-Ori geometries to actuate. It was, therefore, expected that it would give better insight into how changing magnetization orientations affects folding behavior, e.g. a higher sensitivity to the orientation of the driving magnetic torques.

The fully three-dimensional experimental 3×3 panel Miura-Ori structure was modeled in SolidWorks, figure 2. In the fully-three dimensional structure, physical creases were introduced. The creases go through two-thirds the thickness with chamfered edges and the holes are introduced at the vertices, both to reduce interference. The structure has dimensions of 57.2 mm height, 53.1 mm width, and 2.3 mm thickness, with creases thicknesses of 0.77 mm and hole radii of 2.81 mm, all dimensions nominal. The dimensions of the panels are based on Schenk's unit cell geometry [15]. The width and depth of the crease follow Tachi's arguments on the need to promote self-avoidance in finite thickness panels [16]. Note that the creases are alternated up or down to promote folding in the desired mountain or valley orientation.

~~Open face~~ ABS Plastic molds were generated from the negative of the design shown in figure 2(b) using a Dimension® SST 1200ES 3D printer. Mold release agent was applied to each mold prior to the fabrication process. The molds were filled with DOW Sylgard 184 compound and were subjected to a low vacuum of 54 kPa at room temperature (23 °C–26 °C) for 25–30 min using a Model 281A Isotemp® Vacuum Oven connected to a Model TW-1A 1 Stage Vacuum Pump to remove any trapped air pockets. These *substrates* were then subjected to a temperature of 75 °C for 45–50 min to cure and allowed to rest for 24 h before removal from the molds. Twenty substrates in total were fabricated. Substrates were evaluated based on their uniformity in panel thickness. Panels with thicknesses greater than two standard deviations from the mean panel thickness were excluded from experimental testing to remove outliers. Delrin sheets of thickness 0.3 mm were cut to fit panel dimensions (outside the crease zones) and attached to each panel to increase the rigidity of the panels and promote folding at the creases. Delrin sheets were affixed using Loctite Plastic Bonding System two-part adhesive.

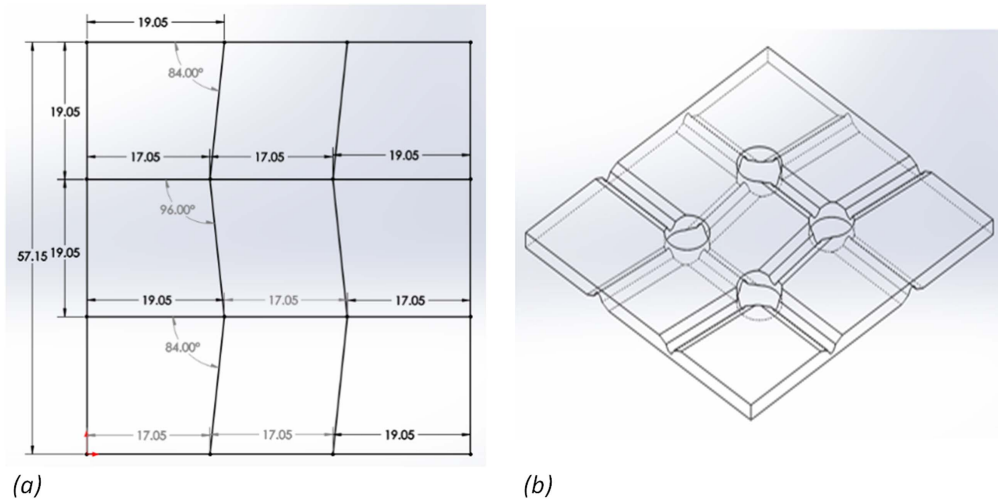


Figure 2. (a) Top view with dimension in mm and (b) isometric view showing crease alternating crease pattern of the Miura-Ori substrate design with nominal hole radii of 3.81 mm and nominal crease thickness of 0.77 mm.

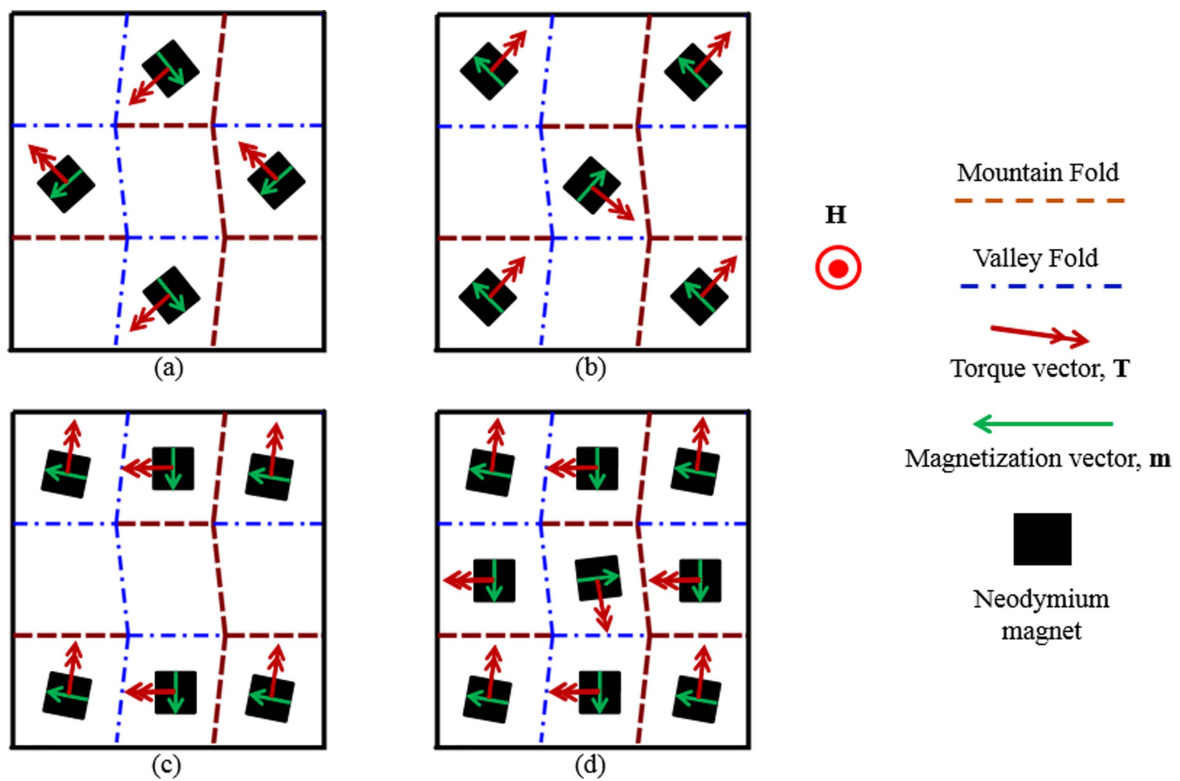


Figure 3. Neodymium magnet placement and orientation for (a) configuration I, (b) configuration II, (c) configuration III, and (d) configuration IV.

2.2. Determination of magnet locations and orientations

The neodymium (NdFeB) magnets used (supplied by K&J Magnetics, model: B222) were Grade N42, 3.175 mm cubes with a high remanent magnetization ($\mu_0 H = \sim 1.2$ T, value given by supplier) in a known direction [17]. The magnets were affixed to the Delrin sheets using the same Loctite adhesive. Neodymium magnets could be placed on any combination of the nine panels in the reduced Miura-Ori.

Furthermore, the orientation of the magnetization of the magnets could be any direction in the plane of the initially flat substrate; out of plane magnetization orientations were not considered. Given these constraints, four initial configurations of neodymium magnet arrangements, panel placement and magnetization orientation within the panel, were chosen after considering both their magnetization, magnetic torque directions, and the actuation of that torque on panels of the Miura-Ori in its initially flat state. The four initial

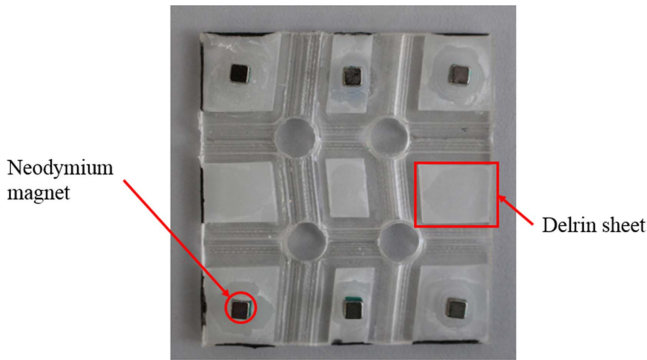


Figure 4. Representative prototype of the magnetically actuated Miura-Ori structure of configuration III. Each panel is affixed with a Delrin sheet; neodymium magnets are then attached in a prescribed direction based on the configurations in figure 3 and table 1.

configurations for study were chosen by the authors as starting points to promote the following conditions based on heuristic arguments:

1. Minimization of the necessary number of magnets for actuation;
2. Initially maximizing the magnetic torque applied to each crease when the fold is flat.

Condition 1 was intended to promote a situation where the fewest numbers of magnets affixed to panels, and thereby affecting adjacent creases, could be employed to distribute torque to all twelve creases. In this sense the torques of all magnets used, when decomposed along the crease lines, impact all twelve creases while placing magnets on the fewest numbers of panels. Condition 2 was intended to maximize the component of the magnetic torque created by each magnet applied to the creases. This measure is directly related to the triple product, calculating the projection of the magnetic torque vectors along the crease vectors.

These conditions lead the authors to four initial configurations, I–IV, chosen initially based on the degree to which magnetic torque was apportioned to each crease. The magnetic torque acting on a given crease can be described by the following scalar triple product:

$$T_k = m_0 H (\hat{m} \times \hat{H}) \cdot \hat{e}_k, \quad (2)$$

where T_k is the torque applied to crease k , m_0 and \hat{m} are the remanent magnetization (assumed constant) and magnetization direction unit vector of the magnet applying torque to crease k , respectively; H and \hat{H} are the applied magnetic field strength and magnetic field direction unit vector, respectively; and \hat{e}_k is a unit vector along crease k . In this work \hat{H} is positive out of the page by definition, e.g. $\hat{H} = [0, 0, 1]$. In figure 3, the magnetic torque vector is shown as a double arrow while the magnetization is shown as a single arrow; initially all magnetizations are wholly in the plane of the page. Note that when the magnetic torque vector is parallel to the crease, magnetic torque on the crease is maximized. When then the magnetic torque vector is perpendicular to the crease, the magnetic torque on the crease is zero.

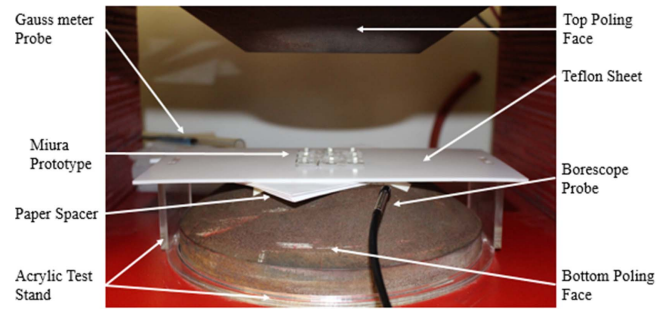


Figure 5. Experimental setup within the electromagnet. The Gauss meter probe extends underneath the teflon sheet (not shown) and is affixed to the top of the bottom poling face. The acrylic test stand and teflon sheet allow the prototype to be rotated 360° but remain in the center of the poling face. Paper spacers were introduced to prevent bowing of the teflon sheet where the Miura prototype was placed.

Configurations I and II arose from condition 1, consisting of only four and five attached neodymium magnets, respectively, placed such that the magnetization directions lie on a diagonal of the respective panels. This provided the minimum number of magnets needed to apply some degree of torque to each adjacent crease. These two configurations represent the same excitation pattern, but with differing boundary conditions. Configuration IV arose from condition 2, having a neodymium magnet aligned such that it applied maximum magnetic torque to a crease. Configuration III is a combination of conditions 1 and 2, limiting the number of magnets while still affecting each crease and maximizing the torque applied to adjacent creases. Three prototypes of each configuration were fabricated by attaching neodymium magnets to the Delrin sheets attached to the substrates using the Loctite adhesive. An example prototype from configuration III can be seen in figure 4.

2.3. Experimental setup

Each prototype was placed on an acrylic test stand within a Walker Scientific 7H electromagnet controlled by an HP E3615A DC power supply connected to an ELGAR 1751SX AC power amplifier. The prototypes were subjected to a magnetic field strength of 0–240 mT at 30 mT intervals. Each field strength was tested three times per crease per prototype, with an accuracy of $\mu_0 H = \pm 0.30$ mT. An Exttech BR350 Borescope and a Canon EOS Rebel T5i Camera (5184×3456 pixels) were used to take image captures of various creases' fold angles, with the borescope probe continually aimed parallel to the crease being measured. This setup is shown in figure 5. Due to the limited space within the magnet only six of the twelve total creases on each prototype were measured. Measured creases are shown and labeled in figure 6. The fold angles of the measured creases were determined using the digital image processing software, ImageJ. The data set per configuration amounted to 432 angle measurements across each of three prototypes' six measurable creases across the range of field strengths.

3. Discussion of results and metrics

3.1. Experimental results

Figure 7 shows representative deformed shapes of a configuration IV prototype within the electromagnet when subjected to increasing magnetic fields. Fold angles for creases 1, 2, 3, 8, 11, and 12 were measured versus field strength for three $H = 0 \dots 250$ mT cycles of each of the 12 prototypes. Note that measured fold angle, θ , ranges from $\theta = 180^\circ$ (flat) to $\theta = 0^\circ$ (fully folded). Results of the measurements are shown in figure 8, but are plotted as $180 - \theta$. Configuration IV shows the highest degree of folding overall while configurations I and III have the lowest degree of folding on average for the vertical and horizontal creases, respectively. Horizontal folds lag behind vertical folds naturally due to the geometry of this Miura-Ori. Combined propagation of measurement error and panel thickness error are computed in the error bars.

3.2. Actuation and idealness experimental metrics

The data collected for each configuration were used to compute two performance metrics: *actuation* and *idealness*. Actuation was calculated from the following equation which averages the results of the six measured creases and normalizes by 180° , providing equal weighting between the vertical creases and the horizontal creases:

$$A(H) = \frac{1}{4} \left(\frac{1}{2} \sum_{i=1}^4 \left(1 - \frac{a_i(H)}{180} \right) + \sum_{j=1}^2 \left(1 - \frac{b_j(H)}{180} \right) \right), \quad (3)$$

where H is the applied magnetic field strength at which the metric A is calculated, a_i and b_j are the set of measured vertical creases and measured horizontal creases, respectively, (θ s measured in degrees) where $i = 1 \dots 4$ and $j = 1 \dots 2$ cycle through their respective sets. The ordered set of creases were

$$a = \{\theta_1, \theta_2, \theta_{11}, \theta_{12}\}, \quad (4)$$

$$b = \{\theta_3, \theta_8\}. \quad (5)$$

All creases start at 180° , $H = 0$, in the Miura-Ori's flat state setting the limits of $A = 0$ in the flat state and $A = 1$ for complete folding. Each test was conducted three times for each prototype yielding the average $\bar{A}(H)$. The comparison of the averaged actuation metrics across the initial four configurations can be seen in figure 9; error bars denote the variance in the fold angle measurements, which is attributed to the method in which the angles were measured and the fabrication variation between prototypes. Configuration IV, which possessed a neodymium magnet on each panel, had the greatest amount of actuation at the highest field strength with $\bar{A} = 0.334$. Configuration II had a normalized actuation factor of $\bar{A} = 0.282$, only 84.4% that of configuration IV. Configuration I and III had the lowest, and almost identical, actuation measures of $\bar{A} = 0.235$ and $\bar{A} = 0.217$, respectively. It should be noted that configurations I and II have similar excitation patterns, one being a diagonally offset version of the other. Therefore, it would be expected that configuration II have 1.25 times the total actuation of

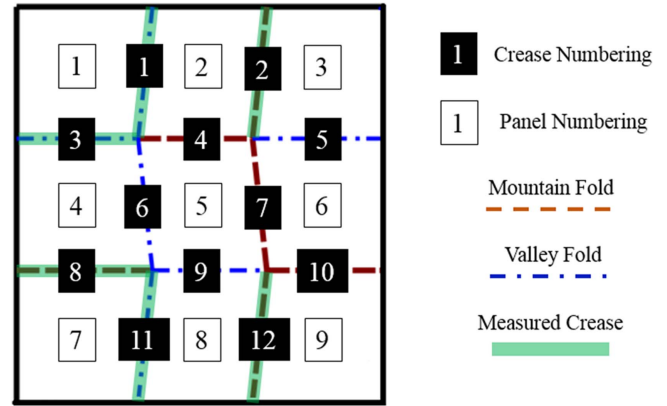


Figure 6. Designated crease and panel numbering of the Miura-Ori. The highlighted creases (vertical creases 1, 2, 11, and 12 and horizontal creases 3 and 8) were measured in the experiment.

configuration I given it has one (out of four) more magnets. From the data, configuration II has 1.20 times the actuation of configuration I, within the error bars of the measured actuation. The results suggest their similarity of excitation pattern extends into similarity of actuation response.

The maximum actuation achieved by each configuration, at a field strength of $H = 240$ mT, is defined as

$$\mathbb{A} = \bar{A}(H_{\max}). \quad (6)$$

The metric for idealness, D , which tests the ability of the prototypes to follow the theoretical, ideal 1-DOF kinematic motion of the Miura-Ori, was calculated from the following equation

$$D(H) = 1 - \frac{1}{2} \left(\sqrt{\frac{1}{6} \sum_{k=1}^6 (1 - d_k(H))^2} + \sqrt{(1 - e(H))^2} \right), \quad (7)$$

where d_k and e are the set of vertical and horizontal fold angle ratios, respectively, at discrete field strength H , and $k = 1 \dots 6$ cycles through the set. The set of fold angle ratios compared within equation (7) are given as

$$d = \left\{ \frac{\theta_1}{\theta_{11}}, \frac{\theta_1}{\theta_2}, \frac{\theta_1}{\theta_{12}}, \frac{\theta_2}{\theta_{12}}, \frac{\theta_{11}}{\theta_2}, \frac{\theta_{11}}{\theta_{12}} \right\}, \quad (8)$$

$$e = \left\{ \frac{\theta_3}{\theta_8} \right\}. \quad (9)$$

These particular comparisons are made since all vertical creases $\{\theta_1, \theta_2, \theta_{11}, \theta_{12}\}$ and both horizontal creases $\{\theta_3, \theta_8\}$ should fold to the same degree at the H th field strength, respectively. Values of the metric range from $D = 0$, not following the ideal fold pattern, to $D = 1$, perfectly following the ideal. Each test was conducted three times for each prototype yielding the average \bar{d}_k and \bar{e} . Making the substitution $d_k = \bar{d}_k$ and $e = \bar{e}$ in equation (7) yielded the average idealness $\bar{D}(H)$.

The idealness at each field strength for each configuration is shown in figure 10. At the maximum field strength, configuration II had the highest idealness, i.e. was closest to ideal, with a value of $\bar{D} = 0.804$. The next highest idealness belonged to configuration I, at 95.5% of configuration II, with a value of $\bar{D} = 0.768$. Configurations III and IV had similar

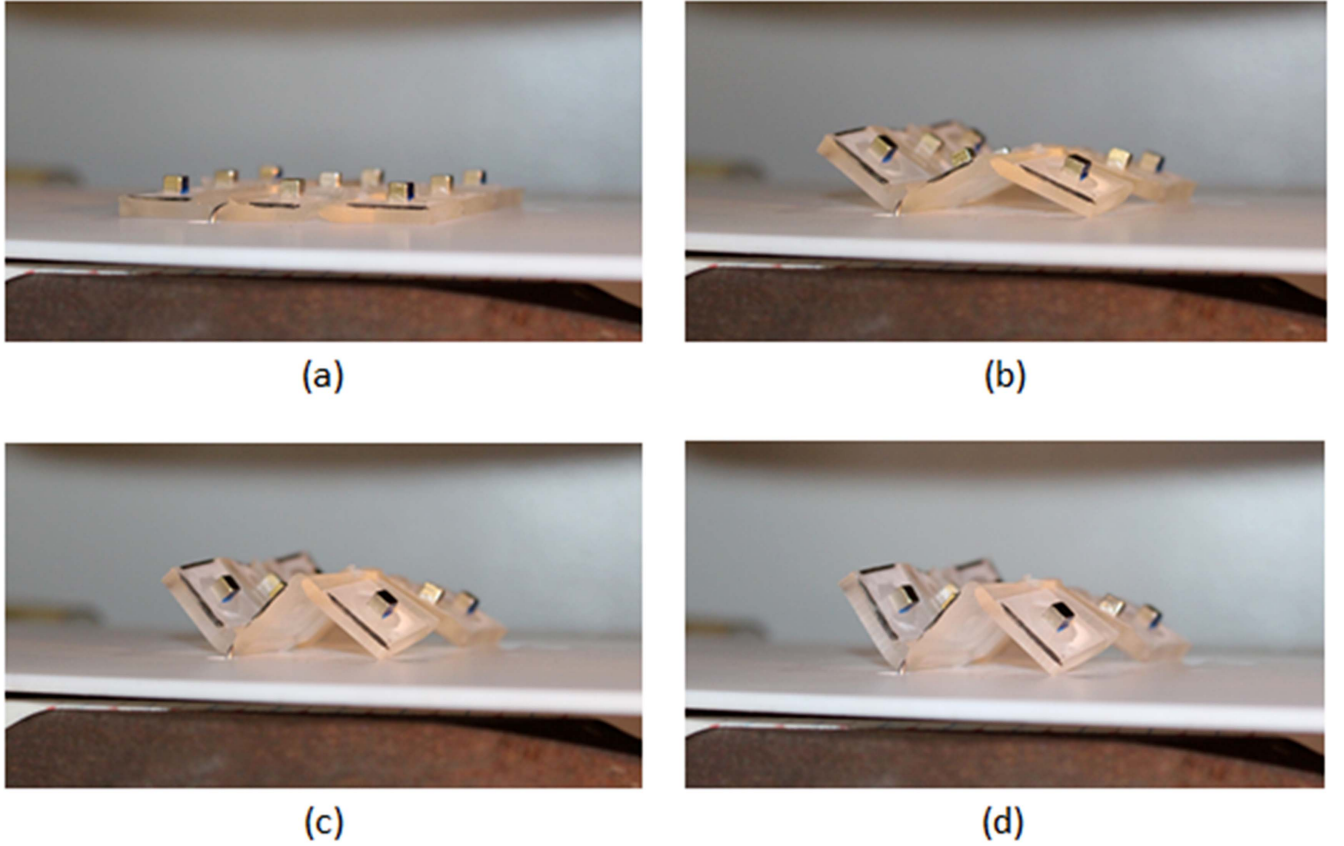


Figure 7. A configuration IV prototype subjected to a magnetic field strength of (a) 0 mT, (b) 80 mT, (c) 160 mT, and (d) 240 mT. Dark lines shown were drawn to assist data collection on each crease.

lower idealness with $\bar{D} = 0.727$ and $\bar{D} = 0.698$, respectively. Trends in the data show that idealness decreases with increasing field strength. Error bars in figure 10 denote the variance in the fold angle measurements, which is attributed to the method in which the angles were measured and the fabrication variation between prototypes and suggest increased variance with increasing field strength as well.

The combined idealness metric representative of the entire structure over its entire range of deformation, consisting of K experimental data points, was computed from equation (10). In equation (10), the idealness value at field strength of 0 mT was excluded given the device is not yet actuated.

$$\mathbb{D} = \frac{1}{K-1} \sum_{n=2}^K \bar{D}(H(n)). \quad (10)$$

3.3. Computational results and metrics

The theoretical magnetic work applied to the Miura-Ori's creases, the last criteria for analyzing the structures, was additionally calculated. Discrete crease trajectories $\hat{e}_k(N)$ for all $k = 1 \dots 12$ creases at N steps were extracted from Zhonghua and Lien's rigid origami folder (ROF) model as the Miura-Ori folded from its initial flat state ($N = 1$), to its completely folded state ($N = 128$) [16–18]; the 3×3 Miura-

Ori pattern with vertical creases six degrees from the vertical of figure 1 was used for computation.

As the origami structure folded, the magnetization vector of a given magnet on a panel rotated with its panel. Using the unit crease vectors as basis functions, it was possible to describe the motion of the magnetizations on each panel completely in terms of crease trajectories, $\hat{e}_k(N)$ and the initial unit magnetization vector \hat{m}_i on panel i adjacent to crease k . Decomposing an arbitrary unit magnetization vector into components in a unit crease vector basis yields:

$$\hat{m}_i(N) = c_{r_i} \hat{e}_{r_i}(N) + c_{s_i} \hat{e}_{s_i}(N), \quad (11)$$

where i denotes the panel in question, \hat{m}_i is the unit magnetization direction vector of the magnet placed on panel i , \hat{e}_{r_i} and \hat{e}_{s_i} are two intersecting crease unit vectors bordering the panel, and c_{r_i} and c_{s_i} are two unknown constants to be determined. Note that the \hat{m}_i , \hat{e}_{r_i} , and \hat{e}_{s_i} vectors all have components described in the Cartesian $\hat{i}-\hat{j}-\hat{k}$ space and vary with step N . Noting also that in the initial flat state all $\hat{m}_i(1)$ are proscribed and

$$\hat{m}_i(1) = c_{r_i} \hat{e}_{r_i}(1) + c_{s_i} \hat{e}_{s_i}(1), \quad (12a)$$

$$\hat{e}_{r_i}(1) \cdot \hat{k} = 0, \quad (12b)$$

$$\hat{e}_{s_i}(1) \cdot \hat{k} = 0. \quad (12c)$$

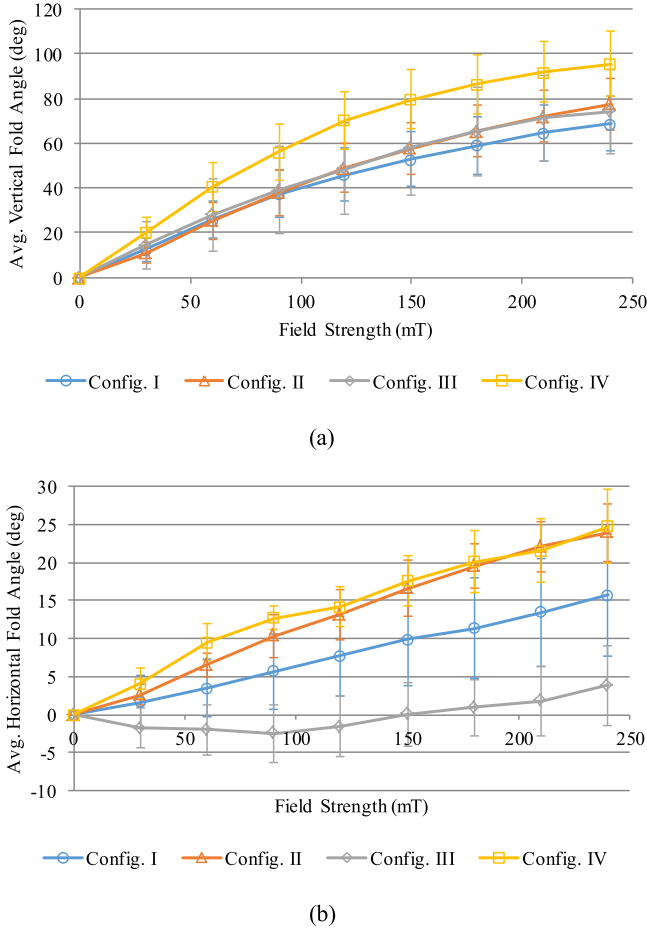


Figure 8. (a) Average vertical fold angles versus applied field strength and (b) average horizontal fold angles versus applied field strength across all prototypes of each configuration; the error bars show the standard deviation. The negative average fold angle values in (b) represent a prescribed mountain and/or valley fold folding into a valley and/or mountain fold, respectively.

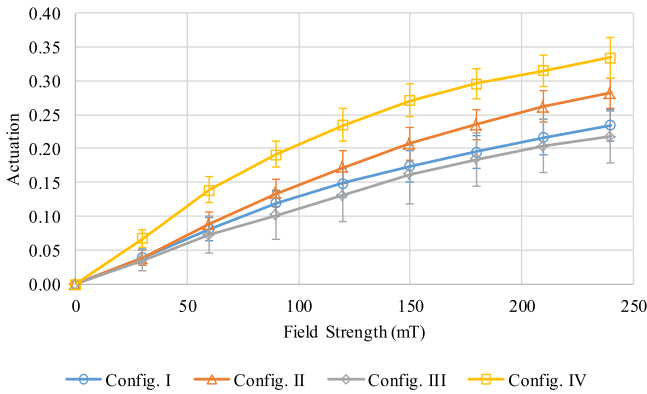


Figure 9. Normalized actuation factor for each configuration.

c_{r_i} and c_{s_i} , specific to panel i , may be found from equations (12a)–(12c) fully defining each \hat{m}_i . With the values of c_{r_i} and c_{s_i} calculated for each magnetization vector on a given panel, the unit magnetization vectors may be computed from equations (12a)–(12c) for any step N .

The ROF crease trajectories, in conjunction with computed unit magnetization vectors, result in the step-wise

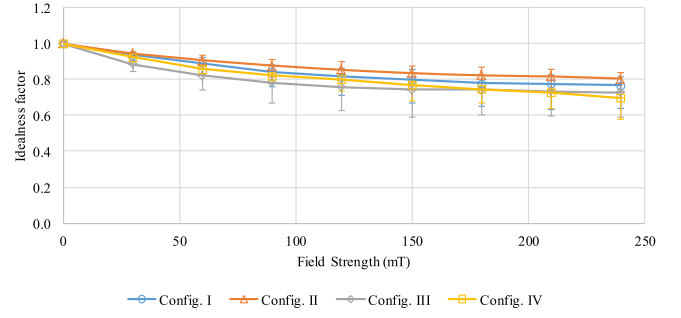


Figure 10. Average idealness factor for each configuration.

discretization of the magnetic torque along a crease from equation (2) as

$$T_k(N) = \sum_{i=1}^9 \alpha_{ik} * m_i * H(N) * (\hat{m}_i(N) \times \hat{H}) \cdot \hat{e}_k(N), \quad (13)$$

where $T_k(N)$ and $\hat{e}_k(N)$ denote the torque on, and the unit crease vector of, crease k , respectively; α_{ik} is the adjacency of panel i to crease k ; m_i is the magnetization of the magnitude of the magnetization on panel i ; and $H(N)$ denotes the value of the applied field strength. Here, N designations define the value of the associated variable computed at discrete computational step N .

Given that not all panels contained magnets or were adjacent to the crease in question, constraints were placed on the contributions of the magnets placed on the Miura-Ori pattern to a given crease. The panel magnetization, m_i , was defined as $m_i = m_0$ if panel i contained a magnet and $m_i = 0$ otherwise. The adjacency condition ensured that only panels adjacent to the crease contributed to the torque on the crease. The adjacency condition for this Miura-Ori structure was defined as

$$\alpha_{ik} = \begin{cases} 1 & \text{if panel } i \text{ is bounded by crease } k, \\ 0 & \text{if panel } i \text{ is not bounded crease } k. \end{cases} \quad (14)$$

The magnetic torque-based work on all creases was calculated by integrating the work performed on creases adjacent to each magnet present in the configuration over the range of deformation. Given the step-wise discretization of the torque, the increment of work was readily approximated as

$$\Delta W_k(N) \approx \frac{1}{2} (T_k(N) + T_k(N+1)) * (\theta_k(N+1) - \theta_k(N)) \quad (15)$$

from which a normalized work metric, numerically integrated over the range of its deformation, was computed as

$$\bar{W}(N) = \frac{1}{\Gamma} \sum_{k=1}^{12} \sum_{N=1}^{128} \left(\frac{1}{m_0 H(N)} \right) \Delta W_k(N), \quad (16)$$

where $\bar{W}(N)$ is the total *theoretical magnetic work* applied to a given configuration through step N , and Γ is the number of neodymium magnets on the configuration. The magnetization m_0 and field strength $H(N)$ in the prefactor of the summation in equation (16) cancel with equivalent quantities in equation (15) once equation (13) has been substituted for $T_k(N)$ and

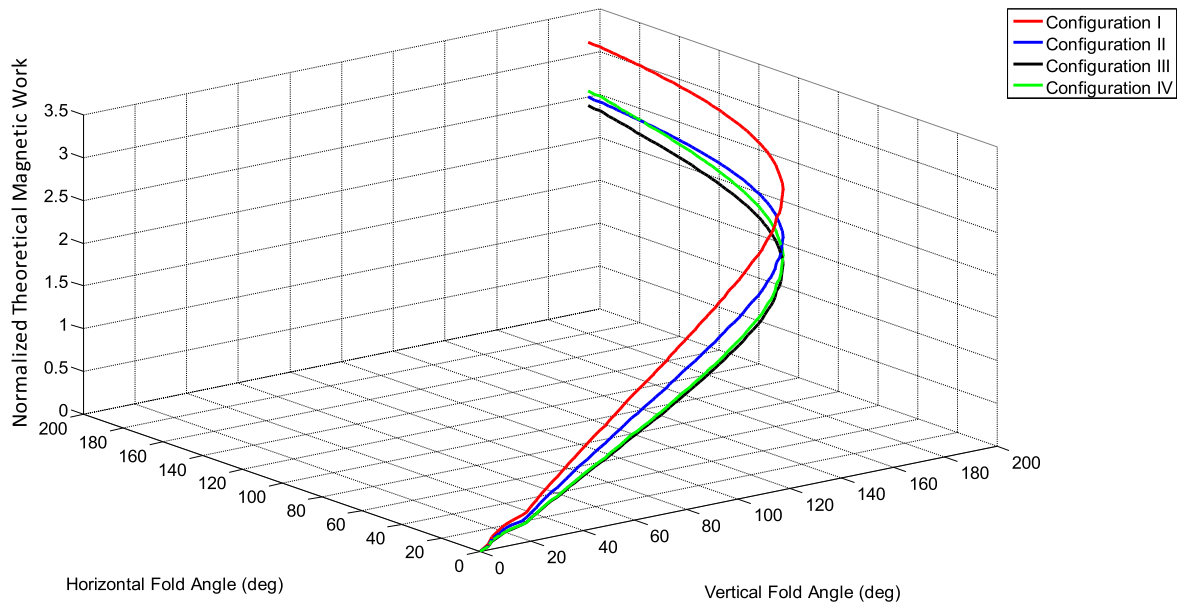


Figure 11. Simulated normalized theoretical magnetic work as a function of horizontal angle and vertical angle. At zero degrees, for both horizontal and vertical angle, the Miura-Ori structure is in its initial flat state; it is completely folded at 180° for both angles.

$T_k(N + 1)$, yielding a metric that is dependent solely on geometry. From equation (16), the combined theoretical magnetic work representative of a given configuration over its entire range of deformation consisting of $N = 128$ computed data points, was simply $\mathbb{W} = \bar{W}(N)$.

With equation (16), the theoretical magnetic work criteria was calculated using the orientations of the magnets in each configuration shown in table 1. Figure 11 shows how the work metric evolves versus deformation of the horizontal and vertical creases for all four configurations. Configurations I–IV had total theoretical normalized magnetic work values of $\mathbb{W} = 3.40, 2.76, 2.66,$ and 2.83 , respectively showing configuration I as superior. It is interesting to note that configuration IV overtakes configuration II for second place only as the structure nears complete folding, highlighting the need to examine behavior along the folding path. Also, observing the total theoretical magnetic work, both configurations I and II have nearly equivalent values. The magnetic work applied to a crease is calculated by the magnetic torque from a magnet applied to an adjacent crease. Due to the diagonal pattern of configurations I and II, each crease has one contribution of magnetic torque, resulting in nearly equivalent total theoretical magnetic work.

4. Trade space exploration

A trade space exploration in which the initial magnetization orientations of the respective neodymium magnets were allowed to vary within a given configuration was conducted to determine which configuration could provide the maximum possible theoretical magnetic work applied to the creases. This was accomplished by utilizing the Army Research Lab's Trade Space Visualizer (ATSV), which allows users to visualize a multi-parameter design space [21–23]. Two cases

were considered: one assuming symmetry, i.e. like panels within a configuration having equivalent magnetization orientations, and another that allowed each magnetization orientation within a configuration to vary independently from the others. The set of equivalent panels in the symmetry trials for each configuration are given in table 2. All magnetization orientations are measured counter-clockwise from the horizontal $+\hat{i}$ in the flat state.

A representative image of each configuration's design space generated within ATSV can be seen in figure 12. Each case shows a relatively clear peak is reached with respect to the variable magnetization orientations. Numerical results of the ATSV trade space exploration are given in table 3 which shows the optimized maximum normalized work value, \mathbb{W}^* , found for a given configuration and its corresponding optimized orientations. Blacked out cells in the table denote that the particular configuration did not utilize the corresponding set of panels. Table 3 shows that the optimized configuration I yielded the highest theoretical magnetic work by a wide margin, $\sim 25\%$. Additionally trade space results for the symmetry cases show improvements in maximum theoretical magnetic work of 53%, 50%, 69%, and 55% over work values for the initially chosen orientation values from table 1 for configurations I–IV, respectively (also see figure 13 columns \mathbb{W} for initial versus \mathbb{W}^* for optimized). For each configuration, trade space results of the independently varying magnetization cases yielded results that showed no improvement in normalized magnetic work over their symmetric counterparts. Therefore, only the symmetric cases are discussed further; magnetization orientations and resulting normalized work results of optimized configurations are denoted with an *. These optimized magnetization orientations, and by extension the optimization process, favor actuation of the vertical creases over the horizontal creases, which can be observed by the resultant magnetic torques

Table 1. Initial (flat-state) magnetization directions in degrees on each panel for each configuration. Angles are measured counterclockwise from the positive x -axis, which points to the right.

| Configuration | Magnetization direction on panel (deg.) | | | | | | | | |
|---------------|---|--------|--------|--------|-------|--------|--------|--------|--------|
| | 1 | 2 | 3 | 4 | 5 | 6 | 7 | 8 | 9 |
| I | | 308.3° | | 228.2° | | 228.2° | | 308.3° | |
| II | 131.8° | | 131.8° | | 51.7° | | 131.8° | | 131.8° |
| III | 174.0° | 270.0° | 174.0° | | | | 174.0° | 270.0° | 174.0° |
| IV | 174.0° | 270.0° | 174.0° | 270.0° | 6.0° | 270.0° | 174.0° | 270.0° | 174.0° |

Table 2. Equivalent panels for magnet orientations in symmetric trade space exploration of configurations I–IV.

| Equivalent panels | Orientation designation |
|-------------------|-------------------------|
| 1, 3, 7, 9 | ψ_1 |
| 2, 8 | ψ_2 |
| 4, 6 | ψ_3 |
| 5 | ψ_4 |

being more aligned with the adjacent vertical creases. The optimization process assumes the complete folding of the Miura-Ori structure and calculates the total work performed once the Miura-Ori is folded. Because the magnetic torque is greatest in the early stages of the Miura-Ori folding, the optimization favors maximizing the work performed on the vertical creases.

The results of the theoretical magnetic work criteria (initial and optimized), in conjunction with the experimentally determined actuation and idealness (initial), were combined into weighted sum models to rank the initial four configurations. The weighted sum model was computed as

$$\mathbb{P} = w_{\mathbb{A}}\mathbb{A} + w_{\mathbb{D}}\mathbb{D} + w_{\mathbb{W}}\mathbb{W}, \quad (17)$$

where \mathbb{P} is the total performance value of a given configuration, and w_i is the relative weight (importance) of criteria $i = \mathbb{A}, \mathbb{D}, \mathbb{W}$ for a given configuration (for the trade space optimized configurations, $\mathbb{W} = \mathbb{W}^*$ and \mathbb{P}^* replaces \mathbb{P}). All \mathbb{W} and \mathbb{W}^* values were normalized by \mathbb{W}_7^* . For the sake of comparison, all criteria are equally weighted: $w_{\mathbb{A}} = w_{\mathbb{D}} = w_{\mathbb{W}} = 0.333$. These weightings would naturally be problem specific, reflecting the importance of any given criteria to the user. Herein the weights serve to illustrate the flexibility of the approach.

Figure 13 shows the experimental (\mathbb{A} and \mathbb{D}) and computational (\mathbb{W}) performance criteria as well as the weighted sum model values (\mathbb{P}) for each configuration based on the initial magnetization orientations. The results of the initial configurations, \mathbb{A} , \mathbb{D} , \mathbb{W} and \mathbb{P} columns, show that configurations I's strong performance in \mathbb{W} overcame its lesser performance in the experimental criteria. The results also show that configuration IV, a close second in the total weighted sum measure \mathbb{P} , scored the highest in actuation \mathbb{A} but was hindered by its weak performance in idealness \mathbb{D} and theoretical work \mathbb{W} . Comparison of the weighted sum models \mathbb{P}^* , which used the optimized work measures \mathbb{W}^* along with the initial \mathbb{A} and \mathbb{D} values for each configuration, again

showed that configuration I* (now denoted * due to its optimization with respect to the work metric) scored the highest due to its still dominant \mathbb{W}^* score. When analyzing the actuation and the total work, normalized work multiplied by the number of magnets, it can be observed that with the exclusion of configuration III, actuation tracks total work. However, the relationship between actuation and normalized work across prototypes is equally, if not more, important.

Following the results of the weighted sum model for the initial and optimized configurations, configuration I was selected for further fabrication and testing. This new configuration, configuration I*, had magnetic orientations corresponding to those in table 3 that maximized \mathbb{W} in configuration I. Consequently, for the \mathbb{W}^* criteria, configurations I and I* are equivalent. Three experimental prototypes were fabricated and tested using the same process as discussed previously. The experimental and computational results for configuration I*, are shown in figure 13. Configuration I* improves upon configuration I somewhat in \mathbb{A} and more significantly in \mathbb{W} , but slightly underperforms configuration I in \mathbb{D} . The weighted sum performance \mathbb{P} of the optimized configuration I* improves upon the weighted sum performance \mathbb{P} of the initial configuration I by approximately 19%.

5. Conclusions

In the construction of active Miura-Ori structures from Delrin on PDMS substrates, four initial configurations of neodymium magnet placements and orientations were determined from heuristic arguments to maximize the utility of the magnets as actuators. Each configuration was experimentally tested for idealness and actuation while the maximum theoretical magnetic work was computed, all as a basis for optimizing the initial structures. Using a weighted sum model, configuration I performed the best and a new configuration, configuration I*, was fabricated and tested based on configuration I's maximum theoretical magnetic work value and its corresponding magnetic orientations. Using the weighted sum model, configuration I* was found further to outperform configuration I by approximately 19%.

From a device standpoint, this work shows that the Miura-Ori pattern may be actuated by magnetic fields acting on discrete permanent magnets as actuators. External magnetic fields can be an effective actuation mechanism, although this effectiveness diminishes as the magnets become more

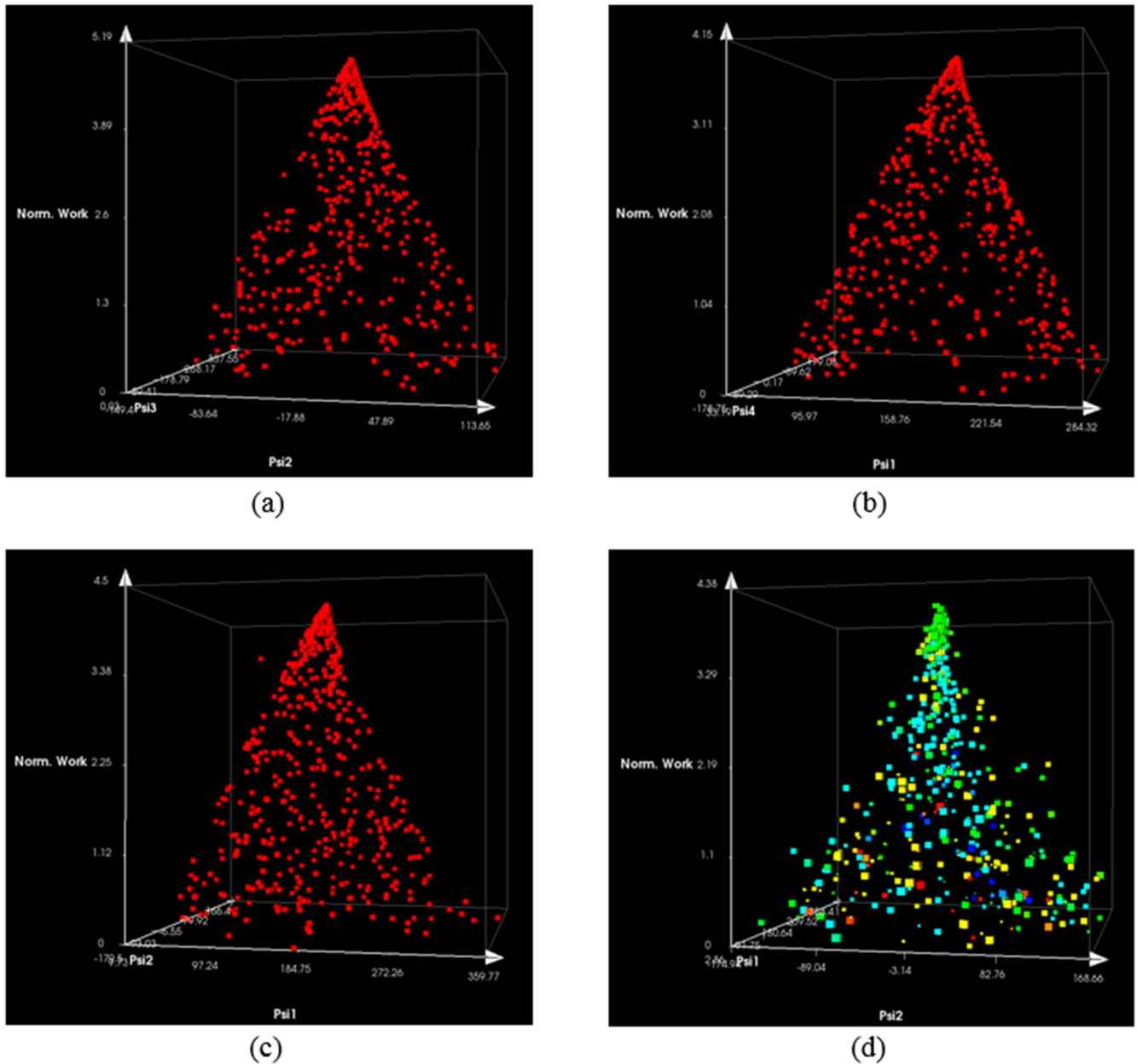


Figure 12. Preference sampler trade space results for (a) configuration I, (b) configuration II, (c) configuration III, and (d) configuration IV. For (d), ψ_3 is defined by the size of the point, small to large mirroring 0° to 360° and ψ_4 is defined by the color of the point, blue to red mirroring -180° to $+180^\circ$.

Table 3. Trade space exploration results of the symmetry cases for the maximum normalized theoretical magnetic work of each configuration with the respective input magnetization orientation values. Angles are measured counterclockwise from the positive x -axis, which points to the right.

| Configuration | \mathbb{W}^* | ψ_1 (deg.) | ψ_2 (deg.) | ψ_3 (deg.) | ψ_4 (deg.) |
|---------------|----------------|-----------------|-----------------|-----------------|-----------------|
| I* | 5.19 | | 353.6 | 187.6 | |
| II* | 4.15 | 173.9 | | | 6.8 |
| III* | 4.50 | 173.5 | 353.1 | | |
| IV* | 4.38 | 169.4 | 353.4 | 210.6 | 25.0 |

aligned with the magnetic field. In order to achieve complete folding, more compliant and wider creases, additional actuators, and/or the introduction of a second magnetic field would be necessary. The inclusion of a metric of the useful work

performed by the actuators (normalized work, \mathbb{W}) highlights an aspect of origami engineering and origami inspired devices that separate them from some traditional devices. In some origami systems, especially the Miura-Ori, actuation is

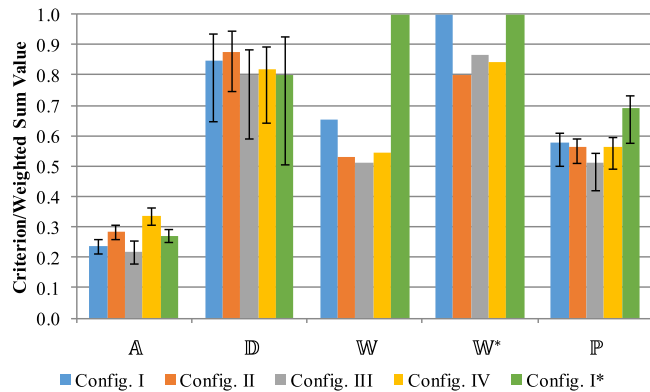


Figure 13. Performance metrics and weighted sum performance values for each configuration. The error bars in \mathbb{P} and \mathbb{P}^* represent the propagation of error from both the actuation and idealness criterion.

severally coupled. In the instance of the Miura-Ori, a single actuator may affect multiple adjacent creases, but the structure itself, if actuated in one location, will respond throughout. In figure 13, column \mathbb{W}^* shows that even though the number of magnets are halved between optimized configurations \mathbb{IV}^* and \mathbb{I}^* , the organization of the magnetic torques in configuration \mathbb{I}^* more efficiently distribute torque to the creases, hence a higher \mathbb{W}^* . This holds true even in the initial configurations \mathbb{I} and \mathbb{IV} . Though they represent the original, heuristic design, and not the optimized case, this is still borne out to some degree by columns \mathbb{A} and \mathbb{D} which show that even though configuration \mathbb{IV} assigned magnets to all nine panels, and configuration \mathbb{I} only to four panels, configuration \mathbb{I} produces better idealness \mathbb{D} . In other words, even with fewer magnets it better reproduces the Miura-Ori folding pattern. It appears that there are diminishing returns with respect to \mathbb{W}^* , as seen in figure 13, when added magnets are introduced to the prototype, despite an increase in total work done. This also suggests that there is a preference for certain panels to have magnetizations, possibly contributing more to the fold pattern than others. Additionally, it should be stressed that configuration \mathbb{I} 's better performance over configuration \mathbb{II} could represent a result of their differing boundary conditions. The authors expect that actuation and idealness differences between \mathbb{I} and \mathbb{II} will diminish as the size of the Miura-Ori structure is increased.

From a design standpoint, this work provides an example framework for the optimization of an active origami structure. Beyond focusing centrally on final target shape approximation (e.g. actuation, \mathbb{A}), this work includes a metric that can be viewed as a sum of incremental target shape approximations (idealness, \mathbb{D}). As engineers work more with origami mathematicians and origami practitioners to develop new devices, the folding paths may become increasingly important in their ability to tune the devices to specific geometry-dependent mechanical or electromagnetic response states. Consequently, while the initial and final configurations are important, the intermediate stages cannot be overlooked. figure 13 column \mathbb{D} suggests, somewhat unexpectedly, that direct actuation of each crease does not necessarily provide

better idealness, though this result may possibly change if idealness were the metric of optimization in the trade space exploration. Moreover, the results of figure 13 columns \mathbb{D} , \mathbb{W} , and \mathbb{W}^* illustrate how optimization of one metric can have undesirable effects on other metrics. This work sought to optimize \mathbb{W} but in so doing reduced \mathbb{D} for its highest-rated configuration. Therefore, it is necessary that future works focus on the optimization between the three criterion (\mathbb{A} , \mathbb{D} , and \mathbb{W}) in order to achieve a more well-rounded prototype.

In a generalized sense, the objective function of an optimization problem defines the goals sought by the designers. In this work, however, optimization was performed only on the normalized work and then used as part of an assessment of the varying configurations \mathbb{I} – \mathbb{IV} and \mathbb{I}^* in a weighted sum model. It is clear that the weights chosen could greatly influence the configuration rankings. If, for example, actuation were more strongly weighted configuration \mathbb{IV} could surpass configuration \mathbb{I} in the initial selection (though its value in \mathbb{W}^* would still hinder its value in \mathbb{P}). The relative values of the weights would necessarily be determined by designers using any of several well-known methods such as analytical hierarchical process.

It should be noted that configurations \mathbb{III} and \mathbb{IV} represent substantive changes in design (e.g. a fully populated configuration in \mathbb{IV} versus an alternating row configuration in \mathbb{III}) which is in contrast to the similar but shifted patterns in \mathbb{I} versus \mathbb{II} . However, both optimized cases in \mathbb{III} and \mathbb{IV} (and those in \mathbb{I} and \mathbb{II}) show similar normalized magnetic work values, \mathbb{W} . The results suggest that the optimization algorithm finds configurations that yield similar utility of the magnets in terms of magnetic work. This is somewhat expected given that across all configurations, respective creases in the idealized Miura-Ori pattern follow the same trajectories. Furthermore, since the magnetic work is dependent on crease orientation with respect to a fixed field, the optimal magnetic arrangement (and thereby the normalized work) could likely be independent of the number of magnets, except in cases when opposing torques are produced. As a design rule, it might then be expected that patterns that provide the minimum number of magnets to apply torque to each crease would be preferred in an optimization of normalized work in that they are least likely to interfere with each other.

Though the scope of configurations in this work was limited to an initial heuristic selection process with a single winner chosen for fabrication and testing using a weighted sum model with uniform weights, future efforts would necessarily include a broader optimization study in which panel selection and magnetization strength as well as orientation are included as an input. Definition of a formal multi-objective function is also needed to broaden the trade space exploration beyond how magnetization orientation and placement affect important metrics. The Miura-Ori geometry and the material of the pattern should be part of the optimization, though the geometry would require generation of arbitrary folding paths in the objective function.

A recent work on similar origami structures by other collaborators has investigated the trade space of water bomb and frog's tongue origami structures actuated with rare earth magnets

[24]. The trade space exploration performed sought the orientation and torque magnitude of magnets placed on each panel while minimizing overall target shape error. While a Pareto front of solutions optimized for this single metric along these two dimensions was found, concepts of efficiency of actuator use were not considered. In this manuscript, tradeoffs between the efficiency with which the final structures engage the affixed magnets, which involves the total torque density and magnet orientation coupled with the path traveled by the magnets during folding, are examined concurrently with more traditional target shape metrics. This type of unified approach is required, especially in the case of magnetic actuation, given that the work performed is dependent on the trajectory of the orientation of the affixed magnets throughout folding. Future efforts by the current authors include development of dynamic models capable of predicting folding paths integrated with trade space optimization that combines traditional target final shape metrics with metrics of intermediate target shape error and actuator work efficiency computed over the complete folding path.

Trajectory may also play an important role considering the effect of interaction between magnets. In this work, simulations were performed to determine the force of attraction between a single pair of magnets versus separation distance (not shown). Using device geometry, and assuming two magnets centered in panels rotating about a crease, the value of the separation distance and the value of the perpendicular distance between the crease axis and the attractive force between the pair of magnets, were used to predict an additional increment in fold angle due to the magnetic interaction (not shown). The additional fold increment at the largest observed fold angle (smallest separation) was less than 1° . Predictions also show that eventually at a 160° fold angle the additional magnetic fold increment reaches 5.25% of the actual fold angle, which can serve as a point of reference for magnetic interactions biasing results.

Using this work as a basis, a more detailed characterization of the Miura-Ori pattern could be created. While the Miura-Ori pattern was the focus of this work, the initial analysis and future improved optimization allows for the utilization in analyzing other origami folds of interest. This would also not be restricted to actuation by way of magnetic material and magnetic fields, but also from other stimuli including electric fields and heat. Overall, the applications of a Miura-Ori structure folded magnetically could encompass a stiffening response to an impact load, as described by Schenk for the Miura-Ori metamaterials [15]. However, this stiffening response could be adjusted in real-time by altering and maintaining a set magnetic field strength.

Acknowledgments

The authors gratefully acknowledge the support of the National Science Foundation (NSF) EFRI grant number 1240459, NSF CMMI grant number 0927326 and AFOSR. Any opinions, findings, and conclusions or recommendations expressed in this

material are those of the authors and do not necessarily reflect the views of the National Science Foundation.

References

- [1] Lauff C, Simpson T W, Frecker M, Ounaies Z, Ahmed S, von Lockette P, Strzelec R and Sheridan R 2014 Differentiating bending from folding in origami engineering using active materials *Int. Design Engineering Technical Conf. & Computers and Information in Engineering Conf. (Buffalo, NY)* [DETC2014-34702](#)
- [2] Zirbel S A *et al* 2013 Accommodating thickness in origami-based deployable arrays *J. Mech. Des.* **135**
- [3] Ryu J, D'Amato M, Cui X, Long K N, Qi H J and Dunn M L 2012 Photo-origami-bending and folding polymers with light *Appl. Phys. Lett.* **100**
- [4] Martinez R V, Carina R F, Chen X and Whitesides G M 2012 Elastomeric origami: programmable paper-elastomer composites as pneumatic actuators *Adv. Funct. Mater.* **22** [1376–84](#)
- [5] Okuzaki H, Saïdo T, Suzuki H, Hara Y and Yan H 2008 A biomorphic origami actuator fabricated by folding a conducting paper *J. Phys.: Conf. Ser.* **127**
- [6] von Lockette Paris R and Robert S 2013 Folding actuation and locomotion of novel planar magneto-active elastomer (MAE) composites *ASME 2013 Conf. on Smart Materials, Adaptive Structures and Intelligent Systems (Snowbird, UT)* [SMA2013-3222](#)
- [7] Landen B, Springsteen K, Frecker M and Simpson T 2015 Optimization of a dynamic model of magnetic actuation of an origami mechanism *Int. Design Engineering Technical Conf. & Computers and Information in Engineering Conf. (Boston, MA)* [DETC2015-47458](#)
- [8] Flores F A F, Susin A A and da Silveira M A 1999 Application of neodymium-iron-boron permanent magnets on the assembling of a novel planar actuator *IEEE Trans. Magn.* **35**
- [9] Satomitsu I and Tsukioka T 2014 A magnetic MEMS actuator using a permanent magnet and magnetic fluid enclosed in a cavity sandwiched by polymer diaphragms *Precis. Eng.* **38** [548–54](#)
- [10] Landen B, Springsteen K, Feldstein H, Frecker M, Simpson T W and von Lockette P 2015 Development and validation of a dynamic model of magneto-active elastomer actuation of the origami waterbomb base *J. Mech. Robot.* **7**
- [11] Miura K 1980 Method of packaging and deployment of large membranes in space *31st Congress of the Int. Astronautical Federation (Tokyo, Japan)* IAF-80 A31
- [12] Miura K 1989 Map fold a La Miura style, its physical characteristics and application to the space science *1st Int. Meeting of Origami Science and Technology (Ferrara, Italy)* pp 77–90
- [13] Horner G C and Elliott M D 2002 A fabrication and deployment approach for a Miura-Ori solar sail model *43rd AIAA/ASME/ASCE/AHS/ASC Structures, Structural Dynamics, and Materials Conf. (Denver, CO)* [AIAA 2002-1708](#)
- [14] Liu S, Lu G, Chen Y and Leong Y W 2015 Deformation of the Miura-Ori patterned sheet *Int. J. Mech. Sci.* **99** [130–42](#)
- [15] Schenk M and Guest S D 2013 Geometry of Miura-folded metamaterials *Proc. Natl Acad. Sci.* **110** [3276–81](#)
- [16] Tachi T 2011 Rigid-foldable thick origami *Origami 5: 5th Int. Meeting of Origami Science, Mathematics, and Education* pp 253–63
- [17] B222 Specification sheet. K&J Magnetics, Inc. Website: <https://kjmagnetics.com/proddetail.asp?prod=B222>

Q2

Q3

- Q4
- [18] Zhonghua X and Lien J-M 2014 Folding origami with closure constraints *Int. Design Engineering Technical Conf. & Computers and Information in Engineering Conf. (Buffalo, NY)* [DETC2014/MESA-35556](#)
- [19] Zhonghua X and Lien J-M 2015 Plan folding motion for rigid origami via discrete domain sampling *2015 IEEE Int. Conf. on Robotics and Automation (ICRA) (Seattle, WA)* pp 2938–43
- [20] Zhonghua X and Lien J-M 2015 Folding and unfolding origami tessellation by reusing folding path *2015 IEEE Int. Conf. on Robotics and Automation (ICRA) (Seattle, WA)* pp 4155–60
- [21] Stump G M, Yukish M A, Martin J D and Simpson T W 2004 The ARL trade space visualizer: an engineering decision-making tool *10th AIAA/ISSMO Multidisciplinary Analysis and Optimization Conf. (Albany, NY)* [AIAA-2004-4568](#)
- [22] Yukish M A, Gary M S and Lego S 2007 Visual steering and trade space exploration *2007 IEEE Aerospace Conf. (Big Sky, MT)* (<https://doi.org/10.119/AERO.2007.352988>)
- [23] Stump G M, Mike A Y, Lego S, Simpson T W and Donndelinger J A 2009 Visual steering commands for trade space exploration: user-guided sampling with example *J. Comput. Inf. Sci. Eng.* **9**
- [24] Bowen L, Springsteen K, Frecker M and Simpson T 2016 Trade space exploration of magnetically actuated origami mechanisms *ASME J. Mech. Robot.* **8** 031012